# CASL Tech Notes

Consortium for Advanced Simulation of Light Water Reactors

August 2013
Volume 1, Issue 3


### About Tech Notes

*CASL **Tech Notes** are produced by CASL's technical staff to spotlight areas of particular technical interest and to discuss CASL science and engineering innovation, accomplishments, activities, and plans.*
***Tech Notes** will be produced on a quarterly basis.*

### In this Issue...


- Model calibration methods for sub-cooled boiling flow
- Modeling irradiation creep and growth
- Exact-to-precision generalized perturbation theory
- On predicting flow stress as a function of strain rate
- Methods for integrating micro-scale creep
- Prediction of hydride formation in zirconium alloys
- Westinghouse CASL test stand update
- Annual student workshop


## Model calibration methods for Sub-cooled Boiling Flow

The majority of CASL's challenge problems involve multidimensional (both spatial and temporal) and multivariate datasets with complex interactivity. To solve these multi-physics problems, different modeling techniques must be applied and the choice of model form (e.g. one-dimensional or multi-dimensional, and model assumptions, e.g. isothermal/non-isothermal, compressible/incompressible) defines the range of phenomena which can be captured by the model equations. Numerical solutions of these equations are often obtained on computational meshes of finite resolution, which further reduces the range of phenomena represented within the solution. The continuum models may be unable to resolve the micro- and meso-scale where many important physics and interactions take place, and a calibrated engineering scale model based on micro- or meso-scale modeling or empirical data may be used to inform the larger solution.

Calibration of these engineering-scale models often relies on statistical approaches where data (observation) uncertainty is accounted for and Bayesian inference plays a central role. However, the complex multi-physics coupling involved and the large number of model inputs and parameters can pose significant challenges to calibration. Unfortunately, for such statistical model analyses the models would need to be run thousands of times, which is impractical in many engineering **(p.6)**

## Modeling Irradiation Creep and Growth with VPSC

During service in a commercial power reactor, the components are subjected to high heat and pressure, and bombarded by radiation. The combination of these stressors causes most materials to deform elastically and plastically over time. For zirconium-based alloys, thermal creep, irradiation creep, and irradiation growth are the primary modes of deformation.

The driving force for thermal creep is high temperature; temperatures greater than approximately 30% of the melting temperature produce high diffusivities of vacancies and interstitials, allowing for their **(p.4)**

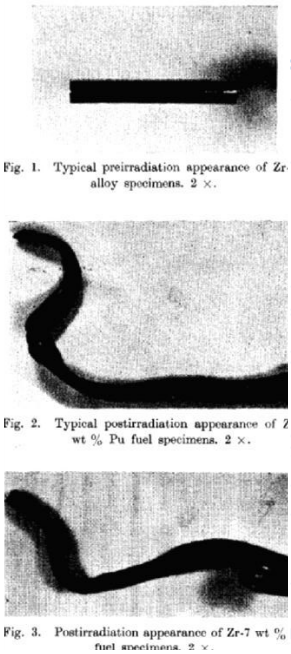

Fig. 1. Typical preirradiation appearance of Zr alloy specimens. 2 ×.

Fig. 2. Typical postirradiation appearance of 2 wt % Pu fuel specimens. 2 ×.

Fig. 3. Postirradiation appearance of Zr-7 wt % fuel specimens. 2 ×.

Experiments in the '60s noted irradiation creep and growth effects [Horak, Rhud, J. Nucl. Mater. 3 (1961)]

## Exact-to-Precision Generalized Perturbation Theory

$E_P$GPT collectively denotes new developments in generalized perturbation theory (GPT) that place an emphasis on computational efficiency in routine design and safety reactor calculations. Over the past several decades, GPT has distinguished itself as a powerful mathematical analysis tool for estimating the variations in system response resulting from general perturbations in the model's input parameters without explicitly solving for the variations in the state variables. Unfortunately, application of GPT is limited by its required computational intensity to estimating first order (i.e., linear) variations of a few selected responses in steady state flux calculations, often excluding thermal-hydraulics feedback and depletion effects.

$E_P$GPT is a hybrid methodology developed at NCSU that combines conventional GPT and a number of other mathematical analyses, including reduced basis methods and range-finding algorithms (RFA). The combination of these methods provide a reduction in the computational cost of calculating the exact responses' variations for a model with many parameters and many responses. The descriptive "Exact-to-Precision" implies a capability that estimates errors in responses' variations, rather than the order of the variations (as currently done by conventional GPT).

Although reactor calculations are inherently complex, past experience has shown that they are primarily dependent on few degrees of freedom (DOFs). When properly determined, these DOFs can be used to recast conventional GPT to more efficiently calculate higher orders of variations. RFA are employed to find the dominant DOFs, while reduced basis methods help recast the adjoint model in terms of a small number of 'active' responses. The active responses are solely dependent on the physics **(p.2)**

*Coming in our next issue of* **Tech Notes**: *Advancements in collaboration and visualization*

## Exact-to-precision. . . (continued from p. 1)

model(s), rather than on the system responses, and are captured by determining the possible state variations resulting from all possible model parameter perturbations. One of the more powerful aspects of the algorithm is that it defines a hard upper-bound on the error. This allows the analyst to decide on the maximum allowable error a priori and employ the algorithm to pick the minimum number, r, of active responses that satisfies the user error criterion.

Several case studies have been completed to demonstrate the application of $E_P$GPT; of particular interest to CASL are the applications to neutron transport and depletion. Reactor design and safety calculations are computationally expensive due to the complexity of the associated physics models; they are nonlinear and coupled with many input parameters and output responses. Some of the applications of $E_p$GPT to radiation transport calculations include development of few-group cross-sections for core wide calculations; the propagation of cross section uncertainties throughout the lattice physics calculations; and the calculation of sensitivity coefficients of macroscopic core responses with respect to input parameters which are necessary to identify key sources of uncertainties and complete data assimilation.

As an example, a 1D two-group heterogeneous diffusion model representing two fuel assemblies was employed to test $E_P$GPT. The state is described by the two-group flux solution. The input parameters are represented by the two-group cross-sections. The model includes 16 cylindrical fuel rods (8 MOX and 8 $UO_2$) moderated by water. For this model, the flux has 256 dimensions representing 128 spatial nodes with equal spatial intervals and two energy groups per node. The reference solution for the system is shown in Figure 1. The $E_P$GPT algorithm was executed, and the cross sections were perturbed randomly using a normal distribution with 10% standard deviation relative to their reference values. The exact perturbed responses were also calculated using direct forward perturbation. Figure 2 compares the relative error[1] of the $E_P$GPT method employing an active subspace of size r=20 and the first-order GPT relative error. The values are ordered such that the first 64 values are the fast flux in the MOX assembly followed by 64 values for the fast flux in the $UO_2$ assembly followed by the thermal flux values. These results indicate that the $E_P$GPT approach can be 3 to 4 orders of magnitude more accurate than first-order GPT.

To study the performance of $E_P$GPT for different sizes of the active subspace, Figure 3 plots the relative root mean square (RMS) error as a function of the active subspace size. For reference, the RMS error calculated by first-order GPT is shown on the same graph as a horizontal line. Analysis of Figure 3 indicates that first-order GPT errors are comparable to $E_P$GPT when the active subspace is too small to properly capture all possible responses variations. As the size the subspace is increased, it starts to capture a larger component of responses variations, and the associated errors are reduced accordingly.

In order to estimate the effect of using the range-finding algorithm, Figure 5 plots the relative RMS error with the upper-bound error predicted by the $E_P$GPT range-finding algorithm. Note that the upper-bound error is consistently higher than the exact $E_P$GPT error calculated by direct forward perturbations until a certain point where increasing

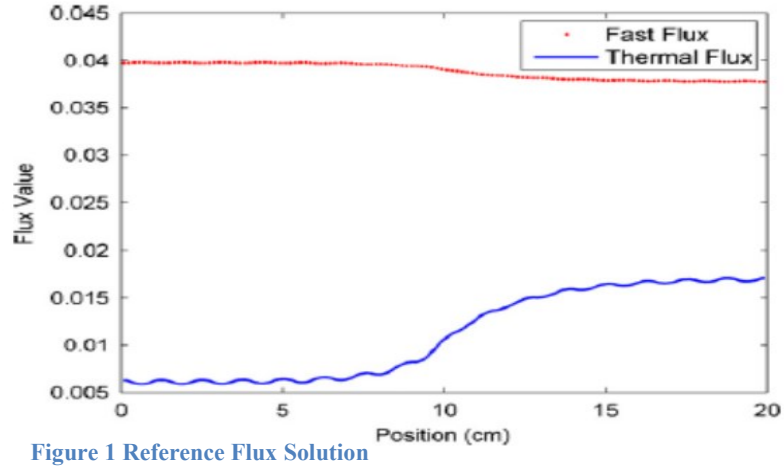


Figure 1 Reference Flux Solution

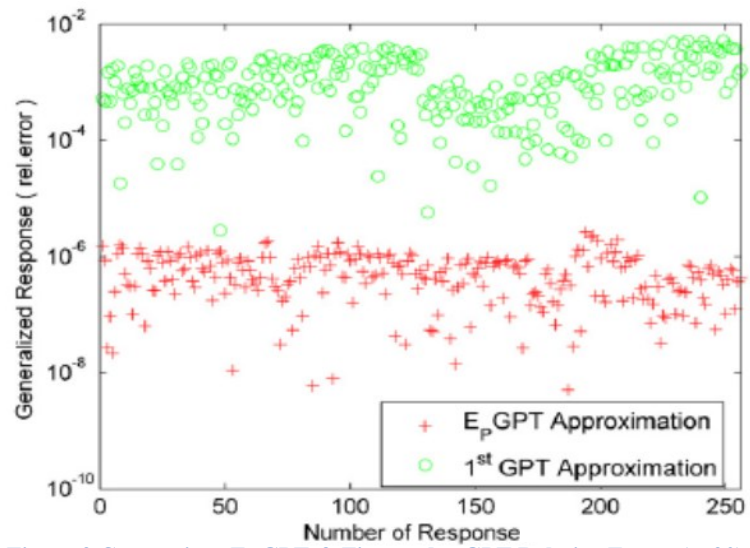


Figure 2 Comparison EpGPT & First-order GPT Relative Error (r=20)

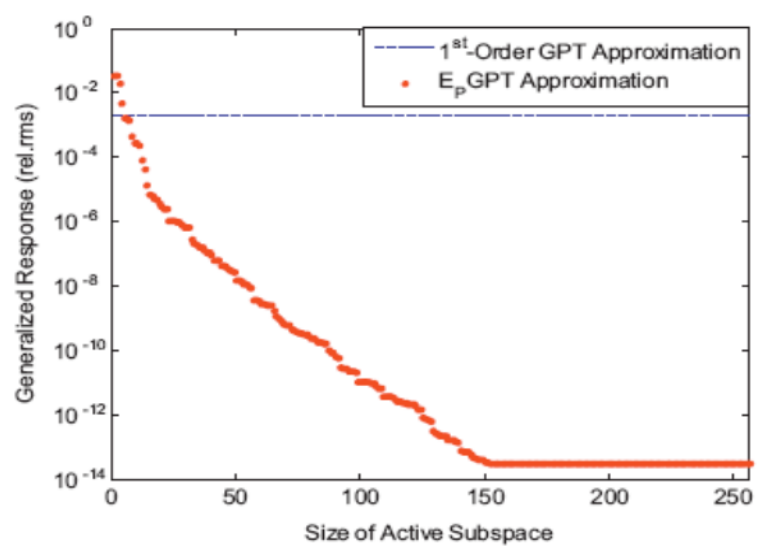


Figure 3 Relative RMS Error for EpGPT and First-Order GPT

the rank does not improve the accuracy of $E_P$GPT estimates. This behavior is attributed to the fact that unlike a source-driven problem, the application of $E_P$GPT to eigenvalue problems requires first an estimate for the eigenvalue which is subsequently used to estimate the responses variations. Any error, however very small, in the eigenvalue estimate will propagate to the responses variations.

To check the adequacy of $E_P$GPT for severe flux variations, **(p. 4)**

[1] The relative error is defined as: (the exact solution with direct perturbation - approximated perturbed solution)/the average reference solution.

# Predicting the Flow Stress of Zircaloy as a Function of Strain Rate

Researchers at MIT and ORNL collaborated to develop a constitutive model, informed by atomistic simulations, that describes the variation of plastic flow stress as a function of temperature and strain rate. The model is important for predicting the plastic deformation of a wide range of metals. While the initial demonstration of the model was completed with iron, the general framework is applicable to zirconium-based alloys used for fuel rod cladding. It allows for molecular -level mechanisms to be probed in strain-rate regimes previously inaccessible to atomistic simulations. The work illustrates that coupled effects of thermal and stress activation can be analyzed naturally in the framework of transition state theory, and provides a parameter-free explanation of the transition from thermal to stress-activation controlled regimes across a critical strain rate range that matches well with experiments.

At low temperature, the deformation of metals is largely governed by the thermal activation of dislocation glide, and experiments on different metals indicate the dislocation flow stress varies with strain rate in an apparently universal manner. The flow stress increases slowly in an Arrhenius manner at low strain rates but turns upward sharply beyond a certain range of strain rate, as illustrated in Figure 4b.

Although the results for different metals can be quantitatively different, the research team postulated that the flow stress "upturn" behavior has a more fundamental origin. In fact, the collaborators derived a general formula to describe a flow stress–strain rate relation that can be applied to predict the dislocation flow stress in single crystals, and demonstrated that their derived formula (Eq. 1) is a good predictor of plastic flow stress in both low and high strain rate regimes as compared with experimental observations.

$$\bar{\sigma}_{\text{flow}} = G\dot{\varepsilon}\,\bar{t} = \frac{\int_0^{\sigma_c} \sigma k(\sigma)\exp[-\frac{1}{G\dot{\varepsilon}}\int_0^{\sigma} k(\sigma')d\sigma']d\sigma}{\int_0^{\sigma_c} k(\sigma)\exp[-\frac{1}{G\dot{\varepsilon}}\int_0^{\sigma} k(\sigma')d\sigma']d\sigma} \qquad \text{Eq. 1,}$$

where σ is the stress, G is the shear modulus, ε is strain, *t* is time, and the dislocation escape rate, *k*(σ), is defined as a function of the escape attempt frequency, *E*(σ).

The derivation takes advantage of general principles that are applicable to a wide range of systems where the reaction rate is time-dependent, while incorporating application-specific boundary conditions. For example, the work was focused on predicting the initiation of dislocation flow (the transition from an elastic deformation regime to a plastic deformation regime) and thus the elastic strain could be utilized. Also, the average residence time is adopted as a means to determine the initiation of dislocation glide. Because the derivation is concerned only with the low-temperature regime (less than 0.15 melting temperature) the dislocation flow activation energy can be taken as equivalent to the activation energy at 0K.

Figure 4(a) shows the predicted behavior based on Eq. (1). Contrary to the conclusions of other studies on the subject, the authors' analysis indicated that the onset of flow stress upturn is attributed mainly to the non-Arrhenius behavior induced by strain rate.

As an illustration of the relative accuracy of the prediction, a comparison with bcc Fe was created. Figure 4(b) shows the variation of flow stress and strain rate at 300 K, as observed experimentally and predicted by the model. Since the magnitude of flow stress is significantly influenced by the defect microstructures in the experimental specimens, a normalized approach is used, and Figure 4(b) presents the normalized flow stress (the ratio of flow stress to its value at the highest strain rate) as a function of strain rate. Both the experiments and Eq. 1 show a significant flow stress upturn in the strain rate range of $10^4$–$10^5$ $s^{-1}$. Quantitative comparisons between experiment and prediction suggest that the proposed correlation can capture the flow stress upturn behavior. This constitutive model has been extended to the strain rate sensitivity term for zirconium alloys in the visco-plastic self-consistent model developed at LANL. The group recently employed the framework to predict the interaction of dislocations with radiation-induced self-interstitial atoms in zirconium over a wide range of strain rates.

For more information on the derivation and approach, see *Onset Mechanism of Strain-Rate-Induced Flow Stress Upturn,* Physical Review Letters 109 135503, 9/28/2012 (Yue Fan, Yuri N. Osetsky, Sidney Yip, and Bilge Yildiz).

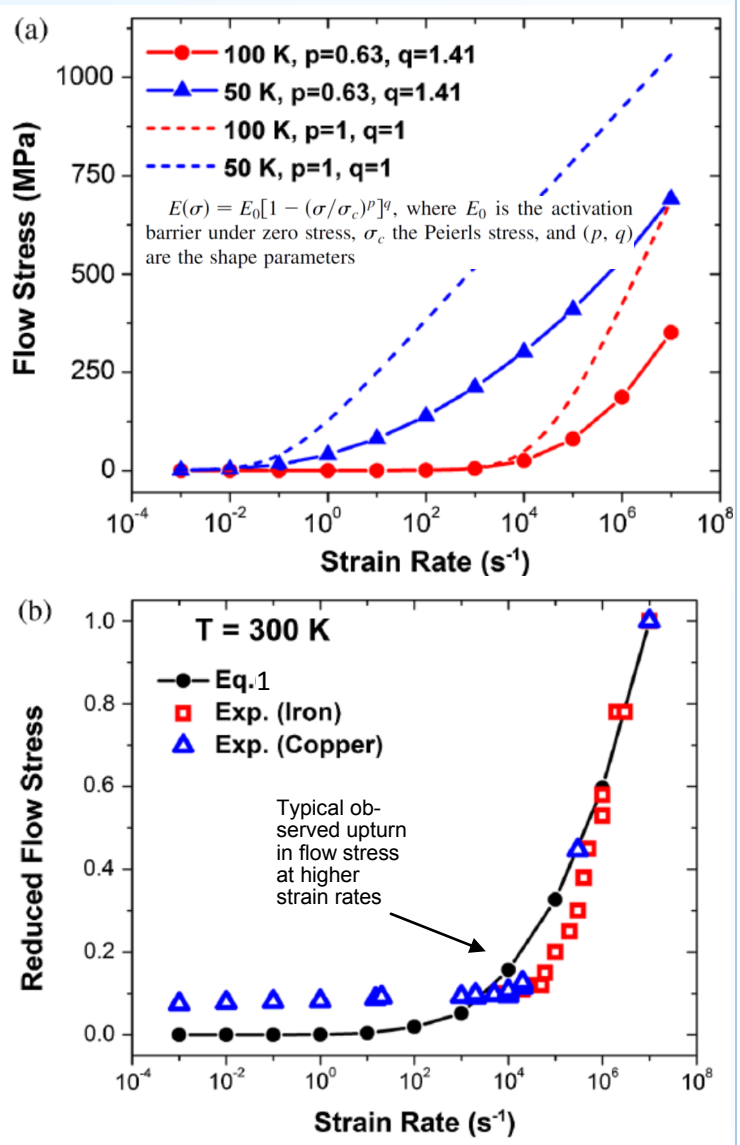


Figure 4 (a) The predicted flow stress versus strain rate at 50 K and 100K. The solid symbols represent the calculated results for the 1/2<111> screw dislocation in bcc Fe. The dashed lines are the results for a hypothetical scenario that corresponds to constant activation volume (*p, q* =1) for the dislocation. (b) Variation of reduced flow stress with strain rate at 300K for comparing experimental results for copper and iron.

## Exact-to-precision. . . (continued from p. 2)

the methodology was also employed to estimate responses' variations resulting from the insertion of a control rod. The control rod was simulated by significantly increasing the absorption cross-section in the middle of the MOX assembly. Similar to the comparison shown in Figure 5 without the control rod influence, Figure 6 plots the relative RMS error with the upper-bound error predicted by the $E_P$GPT range-finding algorithm with an inserted control rod.

In practical engineering calculations when distributed responses do not vary smoothly over the phase space, the number of expansion coefficients is often very large, thereby limiting the practical application of past GPT methods. The $E_P$GPT method provides a less computationally intensive

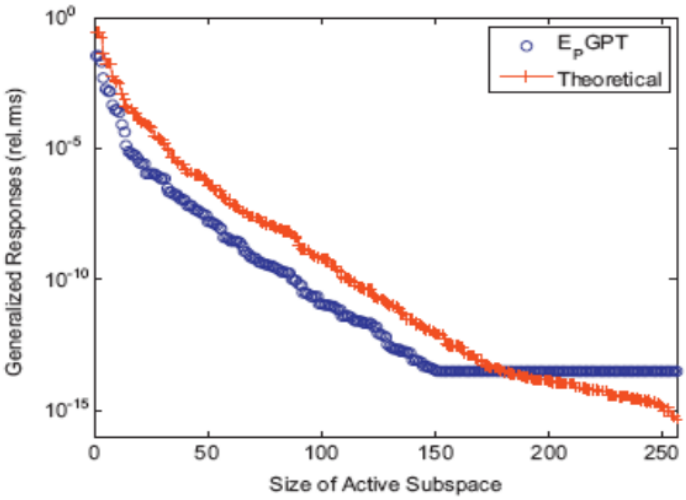


**Figure 5 Relative RMS error with the upper-bound error predicted by the EpGPT range-finding algorithm ("Theoretical")**

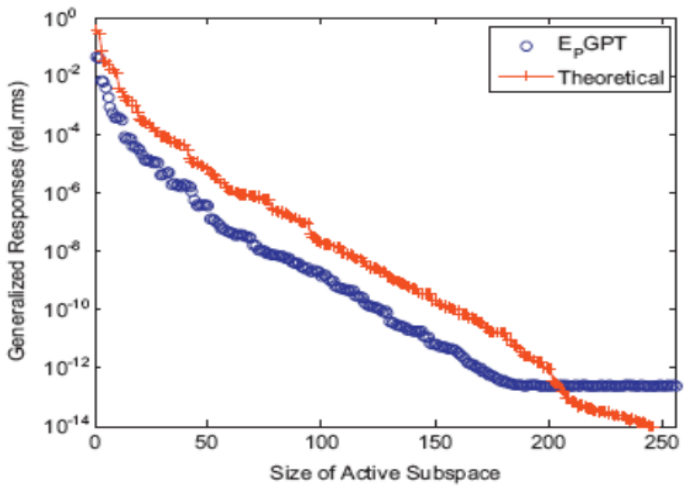


**Figure 6 Relative RMS error with the upper-bound error predicted by the EpGPT range-finding algorithm ("Theoretical") for an inserted Control Rod**

technique that is capable of predicting accurate uncertainty estimates given the expected variation of the model parameters. More information on $E_P$GPT, along with further demonstrations of the method, are available in CASL-U-2013-0010-000, and Nuclear Engineering and Design 256 (2013) 130–140 (C. Wang, H.S. Abdel-Khalik); Exact-to-Precision Generalized Perturbation Theory for Nuclear Reactor Analysis (Congjian Wang NCSU Ph.D dissertation under the direction of Dr. Hany S. Abdel-Khalik); and Nuclear Engineering and Design 241 (2011) 5104–5112 (C. Wang, H.S. Abdel-Khalik).

## Modeling creep & growth. . (continued from p. 1)

preferential absorption by dislocations.

In reactor environments, the neutron bombardment produces a large number of vacancies and interstitials (point-defects). The accumulation of point-defects, known as "sinks," attracts other defects where they recombine and become trapped. In the absence of an applied stress, dislocations present in the lattice preferentially absorb the defects, causing them to climb, and this phenomenon is known as irradiation growth. Irradiation also produces clusters of mobile self-interstitial atoms (SIAs). The SIA clusters are assumed to interact only with dislocations and dislocation loops with the same Burgers vector; consequently, they are the driving force of the anisotropy of irradiation growth.

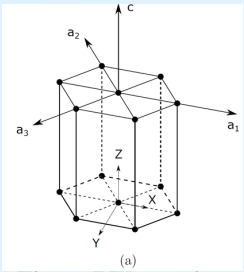


**Figure 7 Illustration of a single crystal of Zircaloy**

When a resolved shear stress is present, the dislocations climb *and* glide, and this phenomenon is known as irradiation creep. Irradiation creep can be induced by irradiation growth: the growth of a grain is opposed by interaction with its neighbors and the resulting stresses induce irradiation creep.

CASL will incorporate a science-based model known as visco-plastic self-consistent (VPSC) to predict irradiation growth and creep. The VPSC approach is a means to predict the macroscopic response of a polycrystalline aggregate, assuming knowledge of the constitutive law of a single grain. VPSC treats each grain as an inhomogeneity included in an effective medium, and iteratively solves for the response of the macroscopic effective medium. LANL and ORNL researchers have incorporated a VPSC crystallographic model of grains and interfaces into a code and are studying the atomistic mechanisms contributing to creep and growth.

The constitutive response of the single grain illustrated in Figure 7 due to creep and growth in its simplest form is:

$$\dot{\varepsilon}_{ij}^{g} = \dot{\varepsilon}_{ij}^{\text{creep}} + \dot{\varepsilon}_{ij}^{\text{growth}}$$

The creep rate for the three types of slip systems (prismatic, basal, and pyramidal) is a function of neutron flux, dislocation density, and applied stress is:

$$\dot{\varepsilon}_{ij}^{\text{creep}} = \sum_s m_{ij}\dot{\gamma}^s = \dot{\gamma}_0 \sum_s m_{ij}^s (m_{kl}^s \sigma_{kl}^s) K^s \left(\frac{\rho^s}{\rho_{\text{ref}}}\right)\left(\frac{\phi}{\phi_{\text{ref}}}\right) = M_{ijkl}^g \sigma_{kl}^g$$

where $\dot{\gamma}^s$ is the dislocation density and $\Phi$ is the neutron flux . The creep rate equation can be transformed to provide the strain rate tensor and resolved shear stress on the system and represents a linear dependence of creep rate with stress, dislocation density and neutron flux.

The creep compliances for each type of dislocation mode, reflecting the most effective creep mechanisms, are:

$$K^{prism} = 10.57\ MPa^{-1};\ K^{basal} = 4.14\ MPa^{-1};\ K^{pyramidal} = 0.11\ MPa^{-1}$$

$K$ can also be regarded as the inverse of a characteristic resistance for moving each type of dislocation. The creep compliances were fit to experimental irradiation creep of Zr-Nb tubes, assuming a constant growth rate for every crystal.

Since irradiation creep is associated with dislocation trapping of irradiation-produced defects, it is expected to increase monotonically with dislocation density and with the number of defects being produced per unit time. The production of **(p.5)**

# Modeling creep & growth. . (continued from p. 4)

defects such as prismatic and basal loops is provided by experimental information as a function of irradiation dose.

To test the model, a single crystal was evaluated with the crystallographic axes aligned with the coordinate axes (see Fig. 7). Fig. 8 (top) shows the normal strain in all three directions as a function of irradiation dose as predicted by the model. The results compare well with empirical results for a single Zircaloy-4 crystal (Fig. 8, bottom). As expected, the irradiation growth model predicts the shrinkage of the crystal along the c-direction, and expansion along the a-directions. The team also investigated the response of textured materials, including rolled Zircaloy-2 and a random texture, both illustrated in Fig. 9. The results, plotted in Fig.10 and 11, are as expected.

Additional modeling is focused on measuring the interaction energy of point-defects with dislocations. The interaction energy is a direct measure of favorability for defect-dislocation interaction. Nine different types of point-defects can be identified in HCP Zirconium. These are listed in Table 1, along with

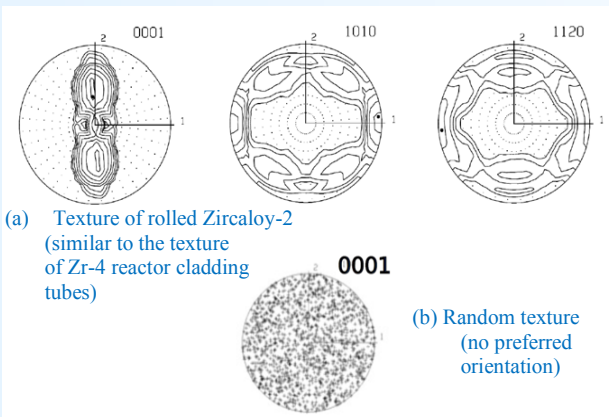


(a) Texture of rolled Zircaloy-2 (similar to the texture of Zr-4 reactor cladding tubes)

(b) Random texture (no preferred orientation)

Figure 9 Pole figures of polycrystal aggregates examined.

their formation energies as identified by the application of the VPSC study and compared with a previous study. The behavior of interstitials in a strain field and related diffusion energy barriers were also studied.

For more information, see *Atomistically informed model of thermal and irradiation creep in Zirconium,* CASL, 10/3/2011 (G. Subramanian et. al.); *Progress report on the incorporation of lower length scales into polycrystal plasticity models,* CASL, 10/15/2012 (G. Subramanian & C. Tome); LA-UR-12-25612.

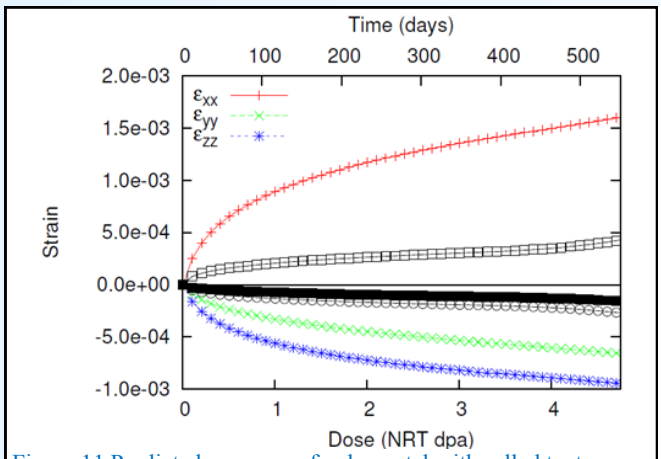


Figure 11 Predicted response of polycrystal with rolled texture, with increased dislocation density. Black symbols are data from Fig. 8.

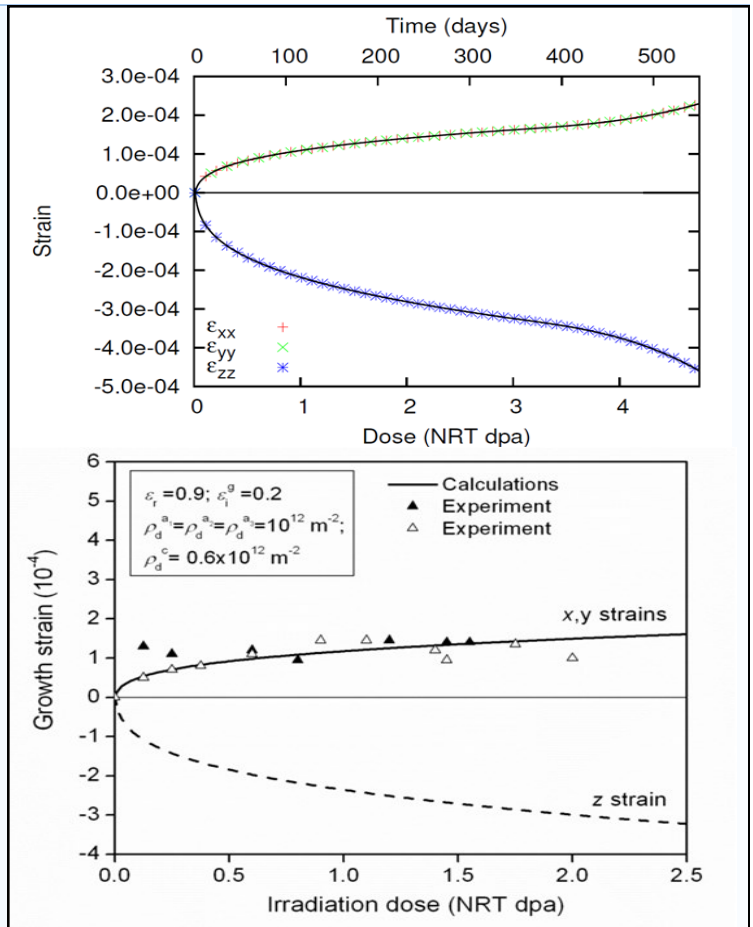


Figure 8 The VPSC-Irradiation growth (top) and experimental measurements on single crystal Zircaloy-4 (G.J.C. Carpenter, R.A. Murgatroyd, A. Rogerson, and J.F. Watters, Journal of Nuclear Materials, 101:28, 1981)

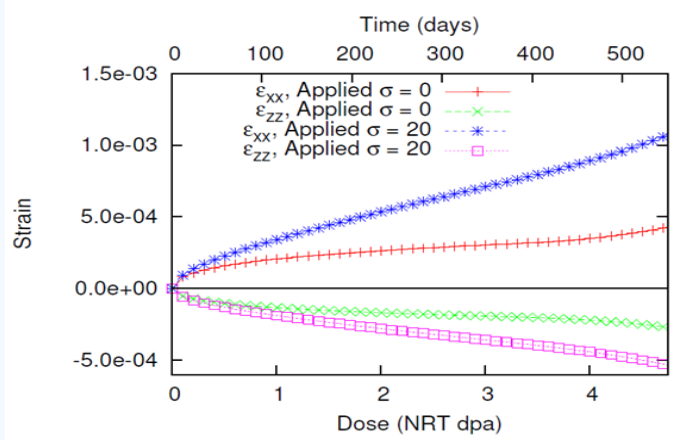


Figure 10 Effect of externally loading the textured polycrystal. Since the load opposes the direction of growth of the polycrystal, the strains in the loaded polycrystal are lesser than the unloaded polycrystal.

Table 1: Various types of point defects in α-Zirconium, and their formation energies [GGA DFT data: F. Willaime, J Nucl. Matls, 323:205, 2003]

| Defect Type | Formation Energy (eV) This study | GGA DFT |
|---|---|---|
| Basal Crowdion (BC) | 2.876 | – |
| Basal Octahedral (BO) | 2.897 | 3.14 |
| Basal Split (BS) | 2.878 | 3.39 |
| Basal Tetrahedral (BT) | – | – |
| Crowdion (C) | 3.135 | 3.52 |
| Octahedral (O) | 2.882 | 3.04 |
| Split (S) | 2.779 | 3.28 |
| Tetrahedral (T) | – | – |
| Vacancy (V) | 1.688 | ?? |

## Model Calibration (continued from p. 1)

applications. In such situations, construction of less computationally expensive surrogates or emulators of the real physical models and application of statistical modeling are needed.

Researchers at Idaho National Laboratory (INL), Los Alamos National Laboratory (LANL), and North Carolina State University (NCSU) joined forces to demonstrate an application of advanced statistical modeling and Bayesian interference methods to calibrate an example multi-physics model of subcooled boiling flows. The variations of the physics and characteristics of subcooled boiling flows are illustrated in Figure 12 and the major constitutive models include drift velocity, mixture-wall friction factor, wall boiling heat flux partitioning, wall boiling nucleation density, wall boiling bubble detachment frequency, wall boiling bubble detachment size, bulk flow condensation, and the flow regime transition model.

The LANL Gaussian Process Models for Simulation Analysis (GPMSA) toolbox was used to calibrate the subcooled boiling model. The GPMSA calibration process includes the construction of a model surrogate using a process convolution technique; execution of computational experiments using the surrogate; construction and training of an emulator; and conducting Bayesian calibration via Markov chain Monte Carlo (MCMC) sampling. The team used a simplified one-dimensional surrogate model derived from the drift flux model to simulate heat and mass transport, and the model calibration was focused on evaporation at the heated wall and condensation in the subcooled bulk flow. Model prediction uncertainty can be caused by both imprecise model form and inaccurate closure models which are usually empirically or semi-empirically derived. Construction of subcooled boiling flow model surrogate was based on 200 simulation runs with the inputs varying over the ranges of interest for the demonstration and based on the conditions of a subset of experimental data used in the calibration.

Using the surrogate model, a computational "experiment" was launched, and the predictions of steady-state 1D axial distributions of void fraction and fluid temperature obtained at 35 spatial locations to construct/train a multi-response emulator. Given the high dimensionality of the outputs, the principal component analysis (PCA) technique was employed to reduce the number of outputs to be surveyed. The void fraction and fluid temperature simulation data sets were separately centered and scaled, and then stacked to create a single matrix of simulated output. The results of applying the PCA technique to the output matrix indicated that up to 99.9% of variance can be captured by the first 5 principal components (PCs) and 99.3% by the first three PCs. Thus, subsequent analyses surveyed the 5 identified PCs.

Next, a multivariate emulator to approximate the real model response is constructed. The representation includes weighting functions and terms to account for the "noise" effect of omitted PCs and any empirical measurement error inherent in the data set. In the Bayesian calibration step, the posterior probability distributions of the considered parameters are evaluated via Markov chain Monte Carlo (MCMC) sampling.

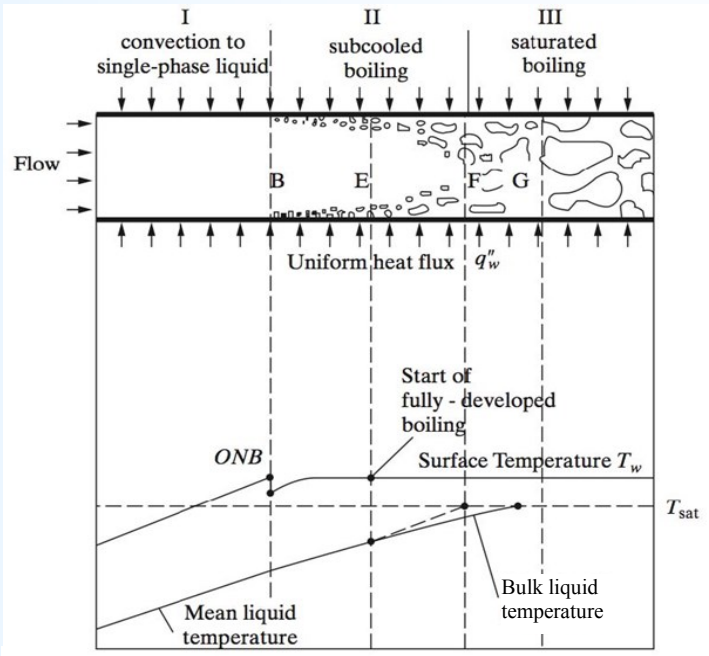


**Figure 12 Variations of heat-transfer mode, flow pattern, wall temperature and mean fluid temperature in a confined subcooled boiling flow without boiling crisis**

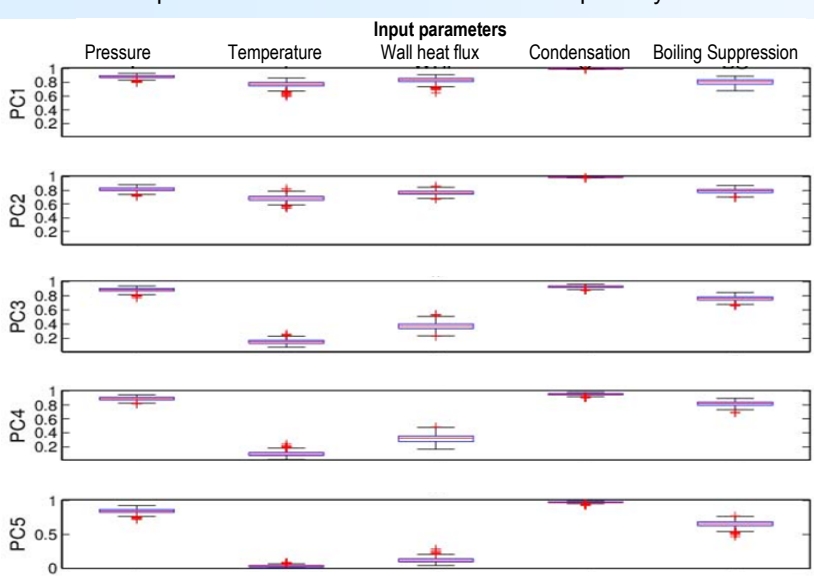


**Figure 13 Boxplots of the marginal posterior distributions.**

Figure 13 shows the boxplots of the distributions for each of the 5 PCs included in the analysis. Values concentrated near 1 for the dominant PCs (such as for the condensation parameter) indicate insensitive parameters. The distributions of the condensation and boiling suppression parameters resulting from MCMC sampling indicated that the boiling suppression parameter is best calibrated to the middle of its range, while the condensation parameter had preferable values near its low limit (zero). A separate sensitivity analysis indicated a small effect of the condensation parameter on the void fraction or fluid temperature responses. Figure 15 provides an example of the calibrated model predictions of both void fraction and fluid temperature at the experimental conditions, along with corresponding predictions of discrepancy and discrepancy-adjusted outputs. These predictions do not account for discrepancy; however, additional analysis found that discrepancy is relatively insignificant at all experimental conditions, suggesting suitable parameters can be found that **(p.7)**

# Methods for Integrating Micro-scale Creep modeling into Finite Element Simulations of Fuel

One of the fundamental challenges of multi-scale modeling is the integration of atomistic-scale effects to continuum scale calculations. For example, the analysis of creep deformation requires continuum-level finite-element calculations to compute local stresses and temperatures which are then used in atomistic models to determine local atom and dislocation response, which feed back to the overall creep response. Due to the complexities involved, different types of analytical approaches are needed at different scales, and establishing a framework where models from different scales are incorporated at the other scales can be a difficult task.

For example, even a numerical look-up table runs into considerable numerical difficulty considering the number of dimensions that such a table needs to be useful. Also, empirical approaches to creep models may obscure insights to the physics mechanism and they cannot be used to extrapolate to new design spaces. As an alternative, the concept of creep-mechanism maps can allow multiple dominant creep mechanisms to be identified and applied in different parts of a component, depending on the local stress state and temperature, and also allows these to change as the local conditions change.

The mechanisms of steady-state creep that are valid when there is no microstructural evolution are diffusional creep (in which atoms diffuse in response to a stress gradient), dislocation glide (in which flow is controlled by the motion of dislocations), and dislocation climb (in which thermal energy provides an additional mechanism for dislocations to overcome obstacles). Each of these laws has a characteristic constitutive relationship between stress and strain rate that can be incorporated into finite-element models. **(p. 8)**

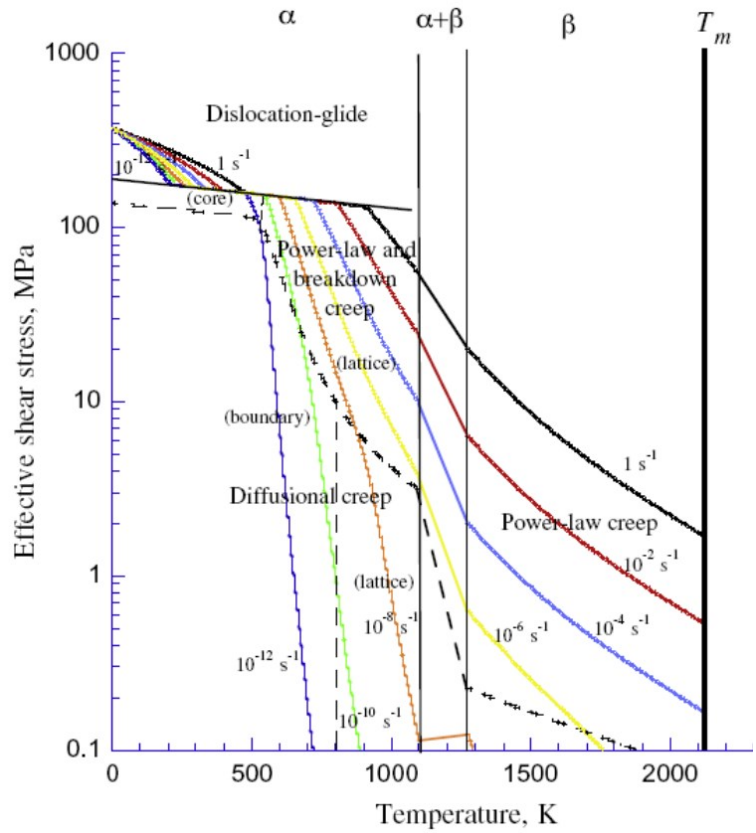


**Figure 14 A deformation-mechanism map drawn using the equations developed for unirradiated Zircaloy-4 with a grain size of 150µm**

## Model Calibration (continued from p. 5)

match the void fraction and fluid temperature data to within the assumed residual errors of 0.07 and 2.0, respectively. Extension of the statistical modeling method proposed to 2D and 3D models is deemed straightforward. Future analyses will include more model parameters and include other datasets relevant to the physics occurring at meso-/micro-scales, and weight factors to characterize data relevancy, scalability and quality would be introduced. More information on this study is available in CASL-U-2013-0101-000 and *Statistical Modeling Support for Calibration of a Multiphysics Model of Subcooled Boiling Flows,* International Conference on Mathematics and Computational Methods Applied to Nuclear Science & Engineering, 2013 (A.V. Bui, N.T. Dinh, R.R. Nourgaliev, B.J. Williams).

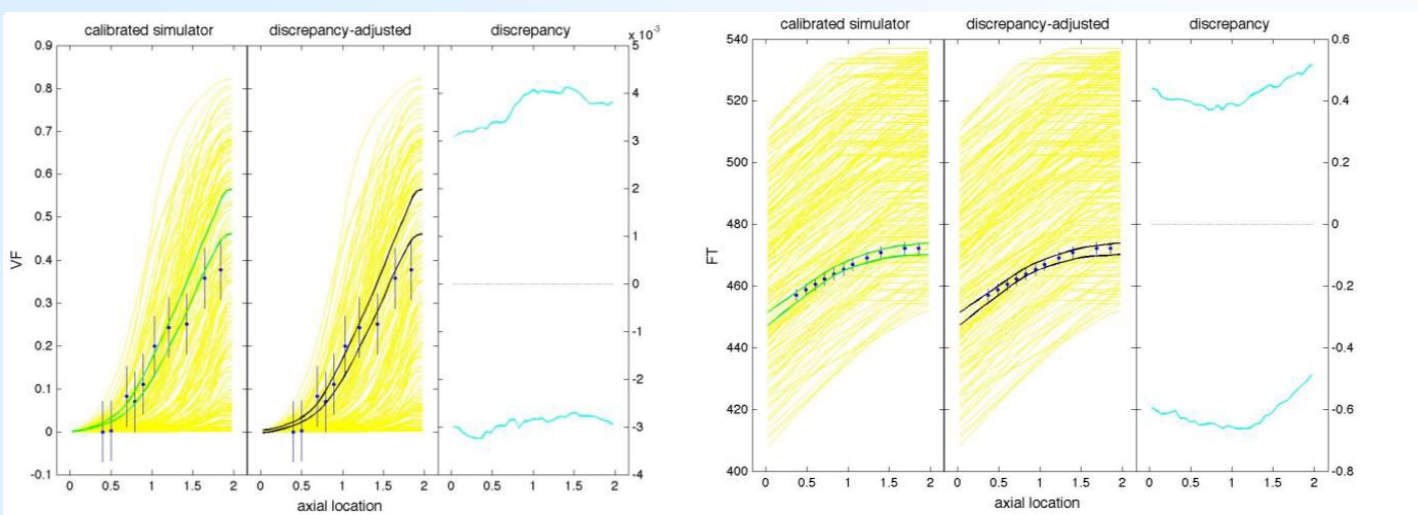


**Figure 15 An example of the study results (experiment 1) 90% pointwise probability intervals from calibrated model (green), discrepancy (cyan), and discrepancy-adjusted (black) posterior processes obtained for void fraction (left panel) and fluid temperature (right panel).**

# Methods for Integrating Micro ..... (continued from p. 7)

A creep-mechanism map is drawn as contours of constant strain rate in a stress–temperature space, as shown in Figure 14. In general, all mechanisms are assumed to act simultaneously, and the boundaries between the different mechanisms are drawn when the dominant mechanisms switch.

As a demonstration of the effectiveness of the creep-mechanism map approach, the constitutive equations associated with each of the dominant mechanisms were implemented within a commercial finite element package (ABAQUS). A Zircaloy-4 tube (thickness 0.024") was modeled as bonded to a cylinder of $UO_2$ fuel (0.315" diameter) with a semicircular chip in it (0.010" depth) as shown in Fig. 16. The equations for the creep mechanisms of $UO_2$ were taken directly from Frost and Ashby[2]; the various creep mechanism models for the Zircaloy-4 were taken from a variety of sources,[3] and incorporated into the finite-element code as a creep-mechanism map. The actual creep rate at any point is determined by adding the rates from all the mechanisms that contribute simultaneously and by selecting the fastest of the mutually exclusive mechanisms. The advantage of this approach is that no a priori assumption about the creep law needs to be built into the FEM code. It is determined on the fly while the calculations proceed. This means that different portions of a structure can exhibit different creep mechanisms, depending on the local stress and temperature. Furthermore the same portion of a structure can exhibit different mechanisms with time, as the stress and the temperature evolve.

The effects of radiation, such as swelling, growth and microstructural changes were not included for either the fuel or cladding for the demonstration, but could be incorporated just as easily if the supporting data exists. The steady-state temperature profile shown in Fig. 16 was developed by applying a power density of 95 MW/m$^3$ to the fuel and fixing the clad surface temperature at 550 K. This steady-state temperature profile was then imported into a 2-D plane-strain finite-element model to calculate the stresses and the creep rates using the creep-mechanism map for the Zircaloy and the fuel. The evolution of the deformation mechanisms with time is shown in Fig. 17.

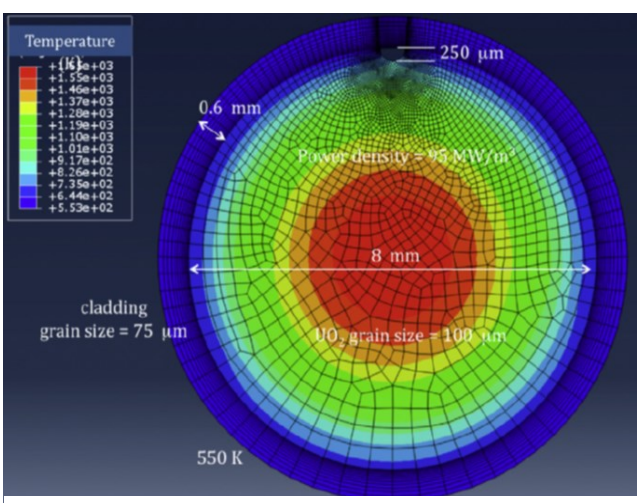


Figure 16 Steady state temperature profile for the cladding and fuel pellet configuration studied

While deformation maps were first conceived and developed more than 30 years ago, they didn't become easy to implement until modern computing capabilities were made available. The frame-work allows the constitutive creep equations appropriate for a particular temperature and stress state to be automatically invoked during a creep analysis. To realize an ultimate goal of multi-scale modeling of a commercial power reactor, additional models need to be developed that link the effects of radiation to creep, including radiation growth, radiation creep, and changes in microstructure.

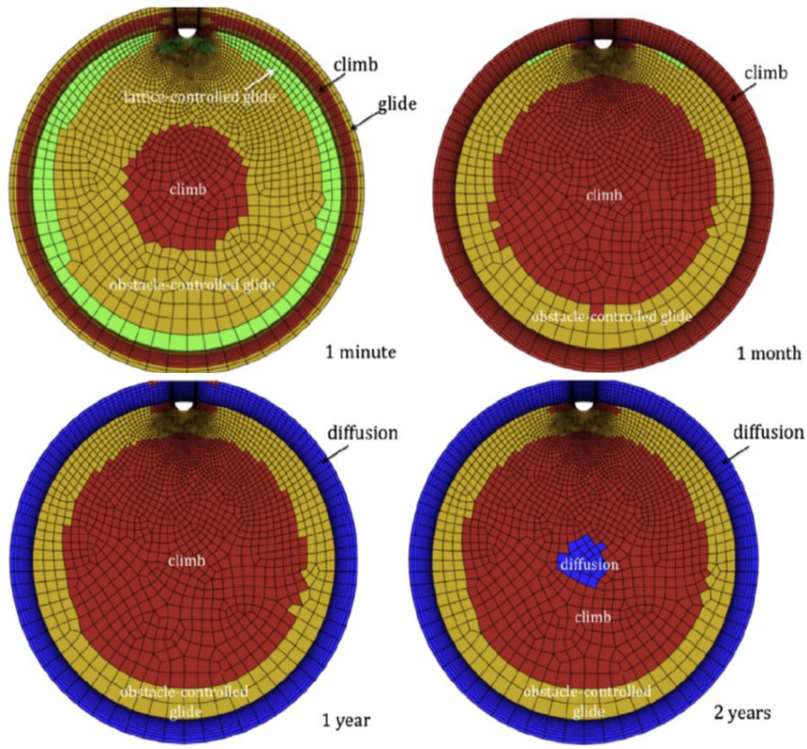


Figure 17 Evolution of deformation mechanisms with time for the cladding and fuel assembly studied

It is likely that this approach can be applied to many multi-scale, multi-physics problems. For example, in the problem of grid-to-rod fretting, different creep mechanisms are needed to calculate deformation of the cladding and relaxation of the contact stresses between the grid and the cladding. An accurate prediction of the changes in geometry and evolution of the contact stresses require an accurate creep model that can efficiently apply the effects of temperature and stress, in addition to radiation effects.

For more information, see *A mechanism-based framework for the numerical analysis of creep in zircaloy-4*, Journal of Nuclear Materials 433 (2013) 188–198 (Hai Wang, Z. Hua, W. Lua, M.D. Thouless).

[2] H.J. Frost, M.F. Ashby, *Deformation Mechanism Maps: The Plasticity and Creep of Metals and Ceramics*, Pergamon Press, Oxford, UK, 1982.

[3] J.L. Derep et. al., *Acta Metall*. 28 (1980) 607–619; C.C. Busby, L.S. White, *Some High Temperature Mechanical Properties of Internally Pressurized Zircaloy-4 Tubing*, WAPD-TM-1243, Westinghouse Electric Corporation, Pittsburgh, PA, 1976; A.T. Donaldson, R.C. Ecob, *Scr. Metall*. 19 (1985) 1313–1318; A.M. Garde, H.M. Chung, T.F. Kassner, *Acta Metall*. 26 (1997) 153–166; D. Kaddour, S. Frechinet, A.F. Gourgues, J.C. Brachet, L. Portier, A. Pineau, *Scr. Mater*. 51 (2004) 515–519; M. Mayuzumi, T. Onchi, J. Nucl. Mater. 175 (1990) 135–142; Y. Wang, *Mechanical Anisotropy of Zircaloy-4: Temperature and Strain Rate Effects*, Ph.D Thesis, North Carolina State University, 1998; S.Y. Lee, K.T. Kim, S.I. Hong, *J. Nucl. Mater*. 392 (2009) 63–69; Y. Matsuo, *J. Nucl. Sci. Technol*. 24 (1987) 111–119; F. Povolo, A.J. Marzocca, *J. Nucl. Mater*. 97 (1981) 323–332; H.E. Rosinger, P.C. Bera, W.R. Clendening, *J. Nucl. Mater*. 82 (1979) 286–297.

# Prediction of Hydride Formation in Zirconium-based Alloys

The formation of hydrides in zirconium alloys is an important phenomenon in the microstructural evolution of LWR cladding materials. The ductility of zirconium-based cladding is strongly related to the size, density, and orientation of hydrides precipitated during the rod's operation, and hydride precipitates can dictate the allowable burnup for commercial fuel rods. To develop a more fundamental, predictive model of hydride precipitation and growth, a phase-field modeling framework, Hyrax, has been developed by University of Michigan researchers for CASL.

The Hyrax framework takes advantage of the INL-developed finite element framework, MOOSE (Multiphysics Object Oriented Simulation Environment). Hyrax includes a nucleation algorithm (based on classical nucleation theory implemented with an enhanced numerical algorithm), a heat conduction model, and a hydride/zirconium misfit strain model to examine precipitation and growth phenomena in a single zirconium crystal. The microstructure is described using a hydrogen concentration and three structural order parameters, with concentration evolution governed by the Cahn-Hilliard equation and structural-order-parameter evolution governed by the Allen-Cahn equation. The effect of elastic strain energy is included via solution at mechanical equilibrium, assuming linear elasticity.

To verify that Hyrax captures classical nucleation behavior, validation studies were carried out against the Avrami equation, both with and without adaptive meshing. Agreement between the Avrami equation and Hyrax predictions demonstrate that the new nucleation algorithm and its implementation within Hyrax accurately captures site-saturation and concurrent-nucleation-and-growth cases. An additional demonstration illustrated the scalability of Hyrax using hybrid parallelism, showing excellent scaling to ~4500 processors. **(p.10)**

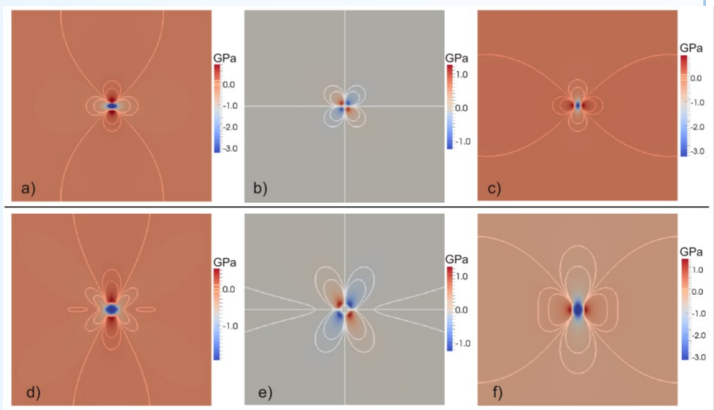


**Figure 18 Stress fields in the hcp basal plane due to the presence of a single δ-hydride (a to c) and γ-hydride (d to f); the contour curves indicate ±50 and ±100 MPa.**

# Westinghouse CASL Test Stand Update

On June 28, CASL successfully deployed selected components of the Virtual Environment for Reactor Applications (VERA) on Westinghouse's industrial computing cluster. Westinghouse is applying VERA to the core physics analysis of the AP1000® PWR. The AP1000 features an advanced first core with a very low leakage loading pattern for optimal fuel cycle cost performance and power distribution. The AP1000 incorporates Westinghouse's MSHIM™ advanced operational strategy, using both black and gray control rod banks during normal operation to reduce soluble boron variations and associated liquid waste effluents, and improving the plant's load following capabilities. These features of the AP1000 core contribute to its overall operational excellence, but also challenge traditional core simulators based on coarse-mesh diffusion calculations with pre-generated lattice parameters. While Westinghouse has successfully addressed these challenges with its state-of-the-art NEXUS core simulator, as noted by Westinghouse Fellow Engineer Fausto Franceschini, the AP1000 first core provides "an excellent benchmark opportunity to investigate the accuracy and practicality of applying VERA and its high-fidelity neutronics components to a advanced core design."

Westinghouse will take a step-wise approach to the VERA test stand simulations, starting with smaller geometries and adding complexity up to full-core calculations. The simulations envisaged for the initial 6-month period of the test stand will culminate in the simulation of the Zero-Power Physics Tests (ZPPTs) for the AP1000 first core, using VERA to calculate control rod worth, isothermal temperature coefficient (ITC) and boron worth. Comparisons with Monte Carlo methods and Westinghouse's NEXUS core simulator will provide important feedback to the CASL team on VERA performance.

Westinghouse has already provided initial feedback to CASL on VERA deployment which, together with forthcoming observations on the performance of VERA for the AP1000 simulations, will provide invaluable information for the CASL team to ensure that VERA is used and useful for the nuclear industry.

Look for updates on the Westinghouse AP1000 simulations in later issues of TechNotes.

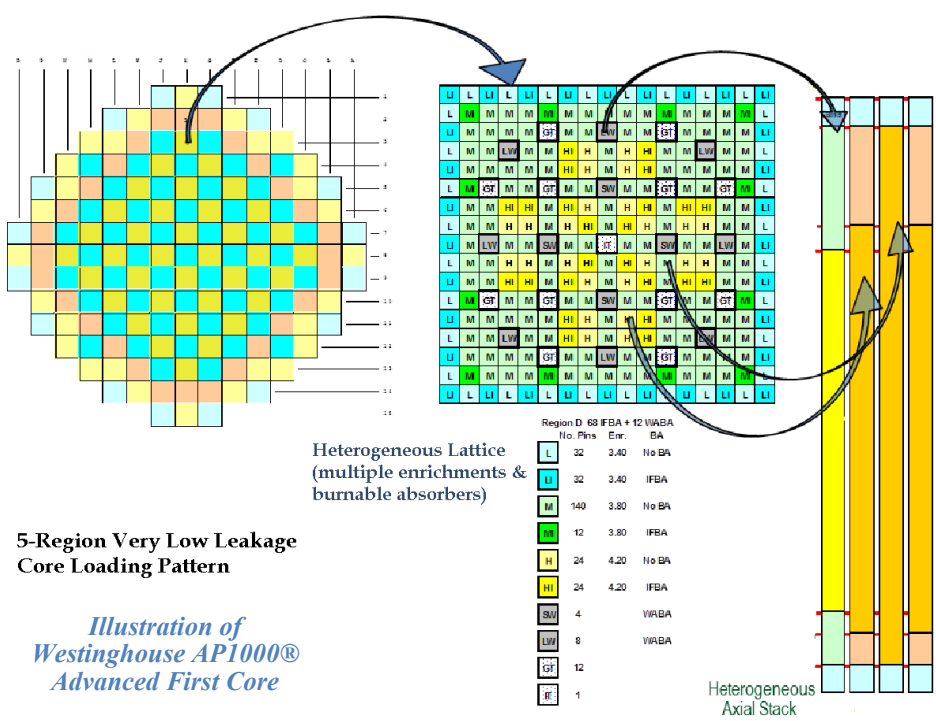


*Illustration of Westinghouse AP1000® Advanced First Core*

# CASL Annual Student Workshop

CASL's Annual Student Workshop, held on July 8-10, was focused on demonstrating the multi-disciplinary nature of the CASL research program and provided a clearer picture of VERA's capabilities. Students from University of Michigan, NCSU, University of Tennessee, Penn State, MIT, Texas A&M, University of Texas, University of Idaho, Virginia Tech, University of Wisconsin, and Florida State University gathered at ORNL to learn more about CASL's virtual reactor environment and the supporting physics codes.

Presentations, given by CASL staff, described development efforts in neutronics, thermal hydraulics, fuel performance and CRUD modeling, and how these efforts are realized in current and future VERA releases. The demonstrations illustrated the importance of coupling neutronics and thermal hydraulic simulations and how this impacts our ability to realistically predict local conditions that effect CRUD formation. Additional presentations were also given as an introduction to the unique modeling and simulation capabilities being developed in CASL and how they will impact future versions of VERA. Students were also given the opportunity to discuss their CASL work in a poster session.

**Student workshop participants, left to right.** (front row) Jun Fang, Murray Thames. (row 2) Cameron Brown, Ezra Ginder, William Gurecky, Benjamin Bond, Andrew Dykhuis, Carolyn Coyle, Jason Hite, Jonathan Walsh, Kylie Jarvis, Ming-jie Zheng. (row 3) Yao Wenquin, Cole Gentry, Daniel Walter, Jia Hou, Alexander Toth, Aron Pawel, David Woodley, Konor Frick. (back row) James Cheung, Mike Short,Taylor Blyth, Erik Walker, Kathryn Biegel. [not pictured: Ondreg Chvala, Kelly Kenner, Travis Lange.]

**Students met in small groups to discuss what they learned from the workshop and provided feedback to improve the experience in coming years.**

# Prediction of Hydride Formation . . .(continued from p. 9)

Several preliminary simulations were performed for hcp zirconium. Figure 18 shows the stress fields in the basal plane of hcp zirconium surrounding individual δ-hydride and γ-hydride precipitates. δ-hydrides have equal misfit strains in the basal plane and a different misfit strain perpendicular to the basal plane, resulting in the formation of platelet-shaped precipitates. γ-hydrides have different misfit stresses in all three axes; thus, needle-shaped precipitates are formed. Figure 19 provides an example of the simulated evolution of an hcp-zirconium and γ-hydrides system obtained from Hyrax.

Future additions to Hyrax will include a free energy functional for zirconium and zirconium δ-hydrides, and it will be applied to examine the terminal solid solubility hysteresis of hydrogen and macroscopic hydride reorientation in three dimensions. The goal for Hyrax is to fully describe the phenomena observed in the zirconium and δ-hydride system. For more information, see *Demonstration of Hyrax Capabilities,* CASL, A. M. Jokisaari and K. Thornton, 3/29/2013.

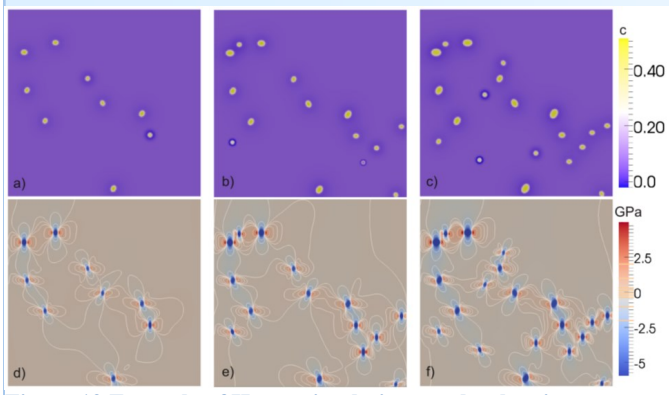


**Figure 19 Example of Hyrax simulation results showing snapshots of evolution of an hcp-zirconium and γ-hydride system (time=6, 9, and 11.7 in simulation time) shown left to right. The sub-figures are a) to c), concentration field; d) to f), $\sigma_{22}$ field.**

**About CASL**

CASL is a DOE Energy Innovation Hub focused on modeling & simulation of Commercial Light Water Reactors. CASL connects fundamental research and technology development through an integrated partnership of government, academia and industry that extends across the nuclear energy enterprise. Learn more at www.casl.gov.

U.S. DEPARTMENT OF ENERGY
Nuclear Energy

**Acknowledgments**

This document is sponsored by the U.S. Government under contract DE-AC05-00OR22725 with UT-Battelle, LLC, which manages the Oak Ridge National Laboratory (ORNL). Accordingly, the U.S. Government retains a nonexclusive, royalty-free license to publish or reproduce these documents, or to allow others to do so, for U.S. Government purposes. Unless otherwise noted, they have been placed in the public domain, although we request the following credit line be used when documents reproduced elsewhere: "Courtesy of CASL, Oak Ridge National Laboratory, U.S. Dept. of Energy.

**Disclaimer**

This document was prepared as an account of work sponsored by an agency of the U.S. Government. Neither the U.S. Government nor any agency thereof, or any of their employees, makes any warranty, express or implied, or assumes any legal liability or responsibility for the accuracy, completeness, or usefulness of any information, apparatus, product, or process disclosed, or represents that its use would not infringe privately owned rights. Further, ORNL is not responsible for the contents of any off-site pages referenced. Reference to any specific commercial product, process, or service by trade name, trademark, manufacturer, or otherwise does not necessarily constitute or imply its endorsement, recommendation, or favoring by the U.S. Government or any agency thereof. The views and opinions of document authors do not necessarily state or reflect those of the U.S. Government or any agency thereof.

**Contact Us:**

**Technical Editor**. . .Rose Montgomery
**Editing**. . . . . .Leslie Nipper
**Distribution** . . . . . .Linda Weltman

Oak Ridge National Laboratory
PO Box 2008, MS6003
Oak Ridge, TN 37831-6003
Email: casl-info@casl.gov

OAK RIDGE NATIONAL LABORATORY
MANAGED BY UT-BATTELLE FOR THE DEPARTMENT OF ENERGY